Experimental Thermal and Fluid Science 136 (2022) 110647

Contents lists available at ScienceDirect

Experimental Thermal and Fluid Science

journal homepage: www.elsevier.com/locate/etfs

Pressure from data-driven estimation of velocity fields using snapshot PIV and fast probes

Junwei Chen *, Marco Raiola, Stefano Discetti

Aerospace Engineering Research Group, Universidad Carlos III de Madrid, Avda. Universidad 30, 28911, Leganes, Spain

ARTICLE INFO

Keywords:
Pressure estimation
Extended proper orthogonal decomposition
Particle image velocimetry
Flow sensing
Data-driven methods

ABSTRACT

The most explored path to obtain pressure fields from Particle Image Velocimetry (PIV) data roots its basis on accurate measurement of instantaneous velocity fields and their corresponding time derivatives. This requires time-resolved measurements, which are often difficult to achieve due to hardware limitations and expensive to implement. In alternative, snapshot PIV experiments are more affordable but require enforcing physical constraints (e.g. Taylor's hypothesis) to extract the time derivative of the velocity field. In this work, we propose the use of data-driven techniques to retrieve time resolution from the combination of snapshot PIV and high-repetition-rate sensors measuring flow quantities in a limited set of spatial points. The instantaneous pressure fields can thus be computed by leveraging the Navier–Stokes equations as if the measurement were time-resolved. Extended Proper Orthogonal Decomposition, which can be regarded as one of the simplest algorithm for estimating velocity fields from a finite number of sensors, is used in this paper to prove the feasibility of this concept. The method is fully data-driven and, after training, it requires only probe data to obtain field information of velocity and pressure in the entire flow domain. This is certainly an advantage since model-based methods can retrieve pressure in an observed snapshot, but show increasing error as the field information is propagated over time. The performances of the proposed method are tested on datasets of increasing complexity, including synthetic test cases of the wake of a fluidic pinball and a channel flow, and experimental measurements in the wake of a wing. The results show that the data-driven pressure estimation is effective in flows with compact POD spectrum. In the cases where Taylor's hypothesis holds well, the in-sample pressure field estimation can be more accurate for model-based methods; nonetheless, the proposed data-driven approach reaches a better accuracy for out-of-sample estimation after less than 0.20 convective times in all tested cases.

1. Introduction

Pressure is a thermodynamic quantity of utmost importance in fluid flows. It performs a key role in flow instability and turbulence, it provides a relevant contribution to the aerodynamic loads, and it is one of the main actors in aeroacoustic noise production, among others. There exists a large wealth of methods to measure fluid pressure, although most of the existing direct techniques are either point-measurements or limited to surface distributions [1].

Remarkably, the increase of time resolution in velocity field measurements during the last decade has opened the path to the possibility of obtaining instantaneous pressure fields [2,3]. This is normally achieved by enforcing the validity of the momentum equation:

$$\nabla p = \mathbf{f}(\mathbf{u}) = -\rho \frac{D\mathbf{u}}{Dt} + \mu \nabla^2 \mathbf{u} \tag{1}$$

which restates the pressure gradient ∇p as a function $f(\mathbf{u})$ of the velocity field $\mathbf{u}$, where μ is the fluid dynamic viscosity, $D\mathbf{u}/Dt$ is the Lagrangian acceleration, expressed as $\partial \mathbf{u}/\partial t + (\mathbf{u} \cdot \nabla)\mathbf{u}$ in the Eulerian approach, and ∇ is the gradient operator.

Particle Image Velocimetry (PIV) has matured as a robust method to obtain the flow-field description needed to extract pressure fields from Eq. (1), in both planar and volumetric domains. However, the hardware limitations of sampling rate often hinder this approach, since high-speed cameras and lasers for PIV are expensive to be available in most of the research and industrial environments, and sometimes they do not offer a high enough sampling frequency for flows of practical interest. Pioneering works on pressure estimation from PIV, thus, were focused on the time-averaged distribution from the Reynolds-averaged Navier-Stokes (RANS) equations [4,5].

For the instantaneous pressure field estimation, in case time-resolution is not available (what is referred from now on as "snapshot PIV"), one possible approach for incompressible flows is to take the

* Corresponding author.
E-mail addresses: junwei.chen@uc3m.es (J. Chen), mraiola@ing.uc3m.es (M. Raiola), sdiscett@ing.uc3m.es (S. Discetti).

https://doi.org/10.1016/j.expthermflusci.2022.110647
Received 27 October 2021; Received in revised form 25 January 2022; Accepted 18 March 2022
Available online 19 April 2022

divergence of Eq. (1), providing that $\nabla \cdot \mathbf{u} = 0$, obtaining

$$\nabla^2 p = -\rho \nabla \cdot (\mathbf{u} \cdot \nabla)\mathbf{u} \tag{2}$$

The main pitfall resides in the boundary conditions. The Poisson equation (Eq. (2)) is an elliptical equation which requires well-defined conditions, either in the Dirichlet or Neumann form, onto the full boundary of the domain. The Neumann boundary condition is generally obtained from the momentum equation (Eq. (1)), thus requiring time-resolved velocity on the boundary or additional assumptions (such as far field conditions) which are often difficult to enforce from PIV data due to the limited size of the measurement domain.

An alternative path to retrieve temporal information relies on model-based methods. In flows with relatively small turbulence intensity and low level of shear, it is possible to exploit Taylor's hypothesis (TH), i.e. assuming that turbulent fluctuations are passively advected with convection speed $\mathbf{u}_c$. This allows estimating the time derivative of the velocity as

$$\partial \mathbf{u}'/\partial t = -(\mathbf{u}_c \cdot \nabla)\mathbf{u}' \tag{3}$$

Previous studies showed that the fluctuations travel with the mean velocity when only small scale motions are present, and the error in such assumption can be less detrimental than noise. However, this cannot normally be assumed in presence of low-frequency, large-scale motions, in which using the low-pass spatially-filtered velocity as $\mathbf{u}_c$ yields more promising results, see [6–8].

A more refined model-based method has been proposed in [9]. The method is based on integrating the inviscid, incompressible vorticity transport equation to estimate the time evolution of the velocity fields, and consequently the pressure field through integration of Eq. (1). The main limitation is that the adopted model is only valid if the full 3D equations are considered, thus it needs 3D PIV measurements as a starting point.

Recent developments on model-free estimation of velocity fields using a limited number of sensors have recently been paving the way to new interesting research avenues to compute the time derivative of the velocity in Eq. (1) without the need of time-resolved field measurements. An interesting approach for time-resolved estimation of velocity fields is based on Extended Proper Orthogonal Decomposition (Extended POD, EPOD). Borée [10] has shown that, when dealing with multiple synchronized measurements, the correlation between them can be ascertained through the evaluation of the extended POD modes which are estimated through the projection of the snapshot matrix of a given quantity on the temporal basis corresponding to another one. This technique reduces to the Linear Stochastic Estimation [LSE, 11] if all the POD modes of the probe data are retained in the reconstruction. The advantage of EPOD with respect to direct application of LSE is that the spatio-temporal correlation is replaced by solely temporal correlations.

EPOD has been already widely used to estimate time-resolved velocity fields from non-time-resolved PIV data and fast probes in jet flows [12], wall-mounted obstacles [13], wake flows [14–16], and turbulent wall-bounded flows [17]. It must be remarked that, in the last decade, the estimation of flow fields from limited probe information has achieved remarkable advances, mainly fostered by an intensive use of machine-learning methods, thus pushing beyond the capabilities of a simple EPOD estimation. Recent advances have been grounded on shallow neural networks [18], convolutional neural networks [19, 20], generative adversarial neural networks [21] and recurrent neural networks [22–24].

In this work, we combine simultaneous snapshot PIV measurements and time-resolved pointwise measurements to achieve the time resolution needed to obtain pressure fields from Eq. (1). The field estimation is carried out using a multi-time delay EPOD formulation. Although more performing methods are already available, this has shown to be sufficiently robust in the time-estimation in case of spectrally compact flows, thus it is considered here a reasonable backbone for proving the concept of full data-driven pressure estimation using simultaneously fast probes and snapshot PIV. The flow chart of the algorithm is shown in Fig. 1.

The EPOD method is introduced in Section 2. Then a robust pressure integration method based on the modified Richardson iteration is presented in Section 3. After that, we illustrate the validation on two synthetic test cases in Section 4, based on direct numerical simulations of the wake behind three cylinders in a configuration referred as fluidic pinball [25] and of a turbulent channel flow from the Johns Hopkins Turbulence Database (JHTDB, 26). Subsequently, the method is tested in Section 5 on PIV experimental data of the wake behind a stalled wing in a water tunnel.

2. Estimation of time-resolved velocity fields with extended POD

In this section the data arrangement and the implementation of the EPOD-based method for the estimation of velocity fields from point probes is presented. The treatment follows the formulation presented in [16]. It is worth to remark that this approach, although defined in the time-domain, is equivalent to a multi-time delay LSE approach [27,28].

Assume that n_t snapshots of the fluctuating velocity field are arranged into a matrix U, where each row (with length $n_p \times 2$ for planar PIV) contains the velocity components in all the nodes of the domain. The matrix U can be decomposed by the economy-size Singular Value Decomposition (SVD), i.e.

$$U = \Psi \Sigma \Phi^T \tag{4}$$

For simplicity it is herein assumed that all grid points cover the same area, thus there is no need to explicitly include a weighting matrix. Furthermore we assume $n_t < 2n_p$. Both conditions are normally met in PIV experiments, where data are most often extracted by cross-correlation with spatially-homogeneous interrogation window size, and the number of grid points is generally larger than the number of available snapshots. Nonetheless, the method can be easily formulated for the general case of non-uniform spatial resolution and/or $n_t > 2n_p$. In the decomposition of Eq. (4), the columns of the $n_t \times n_t$ orthogonal matrix Ψ contains the temporal modes $\boldsymbol{\psi}_i$, the columns of the $n_t \times 2n_p$ orthogonal matrix Φ^T contains the spatial modes $\boldsymbol{\phi}_i$ and Σ is a square diagonal matrix containing the singular values σ_i arranged in a decreasing order.

The same decomposition can be applied on velocity data from s probes synchronized with velocity field measurements. The data from the probes extracted at the same time instants of the PIV measurements can be arranged in a snapshot matrix, with dimension $n_t \times (s \times n_c)$, with n_c being the number of components measured by the probe. In order to increase the quantity of probe data available for each snapshot, a multi-time-delay embedding approach, analogous to the one adopted in [13,29], is employed here: for each physical probe, a time-resolved sequence of q probe samples is extracted after the velocity field sampling time and considered as additional probes, referred for simplicity as "virtual probes". This approach is also known as Multichannel Singular Spectrum Analysis [30]. This method is in wide sense enforcing Taylor's hypothesis, although not explicitly including a model nor imposing a precise convection velocity. The final result is a multi-time delay embedding in the snapshot probe matrix. The final result is a matrix U_{pr} with n_t rows (as the velocity field snapshots) and $n_{tt} = (s \times n_c) \times q$ columns which can be decomposed as

$$U_{pr} = \Psi_{pr} \Sigma_{pr} \Phi_{pr}^T \tag{5}$$

The extended POD modes Φ_e corresponding to the field measurements can be estimated through the projection of the PIV snapshot matrix U onto the temporal modes of the probe, i.e.

$$\Psi_{pr}^T U = \Sigma_e \Phi_e^T = \Psi_{pr}^T \Psi \Sigma \Phi^T = \Xi \Sigma \Phi^T \tag{6}$$

where the subscript e refers to extended POD modes and the matrix $\Xi = \Psi_{pr}^T \Psi$ contains the information about the temporal correlation between field and probe modes.

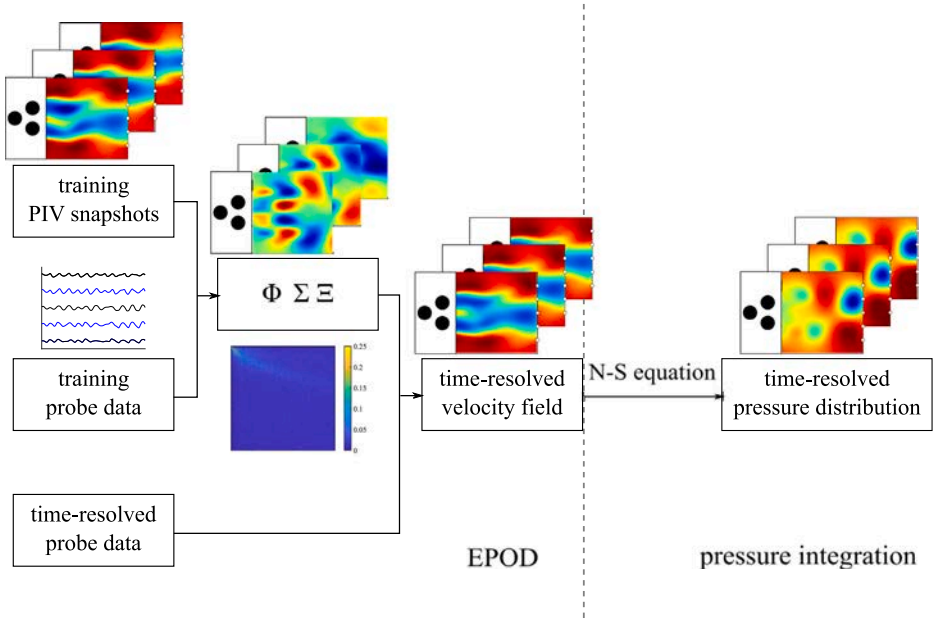

Fig. 1. Flow chart of velocity estimation using EPOD and pressure integration.

Knowing the POD spatial modes (Φ and Φ_{pr}) and singular values (Σ and Σ_{pr}) of the velocity field and of the probe snapshot matrix, as well as the temporal correlations matrix Ξ, it is possible to estimate the velocity field u_{est} at an generic instant from a probe data snapshot u_{se} sampled at that instant:

$$u_{est} = u_{se}\Phi_{pr}\Sigma_{pr}^{-1}\Xi\Sigma\Phi^{T} = \psi_{est}\Sigma\Phi^{T} \tag{7}$$

with u_{se} containing delay-embedded probe data in the same arrangement used to construct the probe snapshot matrix. As shown by Eq. (7), the estimation of the velocity field depends on all the probe modes through the matrix Ξ, accounting also for mode interaction. While this approach removes the need for multiple-time delays (used for instance in multi-time delay linear stochastic estimation [31]), it also might result in a contamination of the estimation from spurious correlations between flow field and probe modes. To this purpose, Discetti et al. [16] proposed to filter out low-correlation entries from the matrix Ξ leveraging on the consideration that uncorrelated random modes might still produce a non-null random entry in Ξ with a standard deviation equal to $n_t^{-0.5}$. The entries Ξ_{ij} in the matrix Ξ are therefore truncated following the 3-sigma rule:

$$\Xi_{ij} = 0,\ when\ -\frac{3}{\sqrt{n_t}} \le \Xi_{ij} \le \frac{3}{\sqrt{n_t}},\ i,j = 1,2,\ldots,n \tag{8}$$

which, on the hypothesis that the spurious-correlation entries follow a normal distribution, guarantees that 99.7% of them are removed. While this approach is robust to noise, it might also cut out a small portion of the actual correlation between probes and flow fields. This is especially critical in the low-data limit, i.e. for small n_t. This approach will be referred to as *Ξ-filtering* approach in the reminder of the paper.

Since the pressure gradient estimation in Eq. (1) heavily relies on a correct estimate of the time derivative of the velocity field, it is of utmost importance to reduce spurious noise in the reconstruction. For this reason, instead of the *Ξ-filtering*, a temporal smoothing of the estimate temporal modes is tested. In the present work a 6th order low-pass Butterworth filter with cutoff frequency equal to 0.05 times the data sample rate is applied to each estimated temporal mode ψ_{est}. This approach will be referred to as *ψ-filtering* approach in the reminder of the paper.

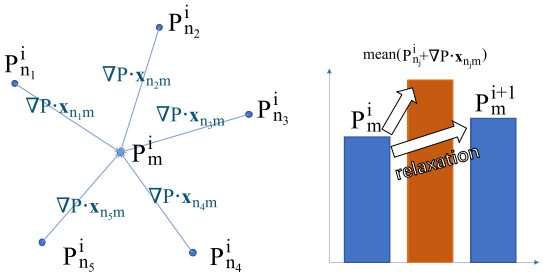

Fig. 2. Left: sketch of pressure update at point m in the *i*th loop of iteration, right: sketch of relaxation.

3. Pressure integration algorithm from velocity field data

Since the time-resolved fields used to compute the Lagrangian acceleration are estimated from point probes, noise amplification is expected in the process. For this reason, a technique with high robustness to noise is implemented for the integration of the pressure gradient. In the last decades, many pressure-integration methods have been investigated using the pressure gradient as a function of velocity. The Poisson approach, based on the resolution of Eq. (2), is the most common one. It has been successfully applied in Refs. [4,32] using Dirichelet or Neumann boundary conditions retrieved from time-resolved velocity field data. The direct integration of the pressure gradient from the momentum equation (Eq. (1)) has been tackled in different ways in the literature. The least-square method, proposed in Ref. [33], seeks the least-square solution for the discrete momentum equation in matrix format. For the spatial integration strategies, in Ref. [34] it is proposed a space-marching integration . Apart from that, several works used an omni-directional integration [35–37], where the pressure is integrated along a bundle of lines starting from the far field and then averaged. An iterative route-independent approach for integration has also been proposed in Ref. [38].

In the present paper, the pressure is integrated using a finite-differences version of the Modified Richardson Iteration method [39], similar to the approach presented in Ref. [38]. As shown in Fig. 2, the pressure in the node m is updated by the value of surrounding point n_j (j = 1,2, …,5) and pressure gradient $\nabla p = \mathbf{f}(\mathbf{u})$ is from Navier–Stokes

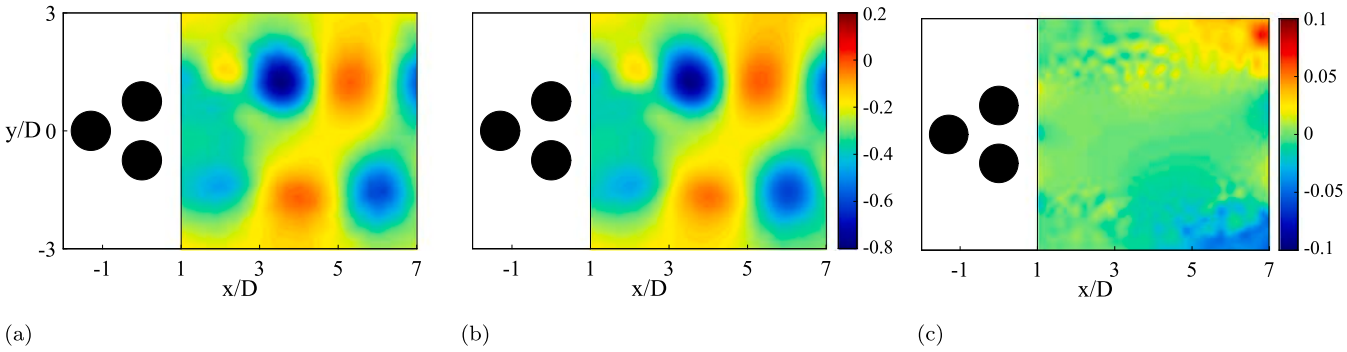

Fig. 3. Geometrical arrangement of the pinball test case and the verification of the pressure integration method introduced in Section 3. Left: (**a**) pressure distribution from DNS (interpolated from original grid to Cartesian grid with grid distance of $0.08D$); (**b**) pressure estimated from the integration method proposed in Section 3, the velocity vectors have been interpolated on Cartesian grid before integration; (**c**) absolute error of pressure estimation. Results are presented in the non-dimensional form $p/\rho U_\infty^2$.

equation (Eq. (1)). The pressure in m at the iteration $i+1$ is provided by

$$\begin{aligned} p^{i+1}(\mathbf{x}_m) =& \frac{1}{N}\sum_{n=1}^{N}(p^i(\mathbf{x}_n) + \mathbf{f}(\mathbf{u})|_{\mathbf{x}'_n}\cdot(\mathbf{x}_m-\mathbf{x}_n)) \\ =& p^i(\mathbf{x}_m) + \frac{1}{N}\sum_{n=1}^{N}(\mathbf{f}(\mathbf{u})|_{x'_n}\cdot(\mathbf{x}_m-\mathbf{x}_n) \\ & - \frac{p^i(\mathbf{x}_m)-p^i(\mathbf{x}_n)}{|\mathbf{x}_m-\mathbf{x}_n|}(|\mathbf{x}_m-\mathbf{x}_n|)) \\ =& p^i(\mathbf{x}_m) + \frac{1}{N}\sum_{n=1}^{N}(\mathbf{f}(\mathbf{u})|_{\mathbf{x}'_n} - \nabla p^i|_{\mathbf{x}'_n})\cdot(\mathbf{x}_m-\mathbf{x}_n) \end{aligned} \tag{9}$$

where i is the index of iteration, $\mathbf{x}$ is the position of each point, N is the number of neighboring points (for a Cartesian grid, 4 in 2D, 6 in 3D), among which points in the other side of boundary do not count, and the gradients are calculated in the middle point $\mathbf{x}'_n = (\mathbf{x}_m + \mathbf{x}_n)/2$ to reduce truncation error. Then, a relaxation parameter $\omega < 1/N$ is introduced into Eq. (9), which becomes

$$p^{i+1}(\mathbf{x}_m) = p^i(\mathbf{x}_m) + \omega\sum_{n=1}^{N}(\mathbf{f}(\mathbf{u})|_{\mathbf{x}'_n} - \nabla p^i|_{\mathbf{x}'_n})\cdot(\mathbf{x}_m-\mathbf{x}_n) \tag{10}$$

The process is initialized with $p^0 = \mathbf{0}$, updates globally in each iteration, and terminates when the difference between the pressure in two loops is below a threshold ε, i.e. when $\|p^{i+1} - p^i\|_2 < \varepsilon$, where $\|\cdot\|_2$ is the $\mathcal{L}^2$ distance over all the points of the domain and the threshold (set to 10^{-5} for the present study) is determined accordingly to the maximum accuracy of pressure that can be attained depending on velocity field data precision. The relaxation parameter ω has been set equal to 0.1 in the remainder of the paper. Additionally, a threshold on the maximum number of iterations is set to be 10^4.

The main differences with the method proposed in Ref. [38] reside in the update process. In Ref. [38] the pressure in x_m is updated considering only the surrounding nodes, i.e. $p(x_m)$ is not included. Furthermore the data are updated instantaneously within in each iteration. In our test, the performance of the robust iterative method in this section prevails under noise condition.

4. Validation

In this section a validation using synthetic datasets is carried out. To this purpose we selected two test cases with substantial spectral difference, i.e. a shedding-dominated flow (Section 4.1) and a wall-bounded flow (Section 4.2).

4.1. Fluidic pinball

The first synthetic dataset has been extracted from a 2D-DNS (2 Dimensional Direct Numerical Simulation) of the wake of a *fluidic pinball* [25]. The pinball is formed by three cylinders with diameter D, whose centers form an equilateral triangle with side length equal to $1.5D$. The triangle is oriented with one vertex pointing upstream, as illustrated in Fig. 3. The 2D-DNS is performed at $Re = 130$ (referred as chaotic regime, [25]), with Re being the Reynolds number based on the freestream velocity and the diameter of the cylinders forming the pinball.

The region selected to test the EPOD-based estimation is placed in the wake of the obstacles, ranging from $x = 1D$ to $x = 7D$ and from $y = -3D$ to $y = 3D$, with x and y being respectively the streamwise and crosswise directions. The velocity data from the original DNS mesh are interpolated on a Cartesian grid with distance between two adjacent points of $0.08D$ in order to simulate the results of a PIV experiment, yielding 76×76 vector fields (although neither modulation nor random errors are introduced). The pressure field obtained on this Cartesian grid using the method presented in Section 3 is reported in Fig. 3. It can be observed that the integration error is relatively small, except for the corners of the domain, where the truncation error from the interpolation becomes significant.

Five point probes measuring the 2 in-plane components of velocity, are placed at the downstream edge of the region ($x = 7D$), with a spacing of $1D$ in the y direction, being the central one located at $y = 0$. The training dataset is composed of 4685 velocity field snapshots as well as of the synchronized virtual probe data, forming the matrices U and U_{pr}, respectively, as reported in Section 2. The snapshots are selected to have a temporal spacing of 1.9 non-dimensional times. The probes, instead, store data with the same time separation of the DNS advancement, i.e. each 0.1 in non-dimensional time units. This corresponds to a target super-sampling by a factor of 19. When building the probe snapshot matrix, a time segment equal to 60 samples is used. The number of virtual probes is estimated by considering a timespan covering the convection time through the observation domain, as proposed in Ref. [16].

Fig. 4a reports the energy distribution of the POD modes σ_i^2 of the velocity field snapshots with blue line, as well as the cumulative energy distribution with red line. As expected for this shedding-dominated flow, the first few POD modes contain most of the energy, with over 95% of the total energy contained within 12 modes. Fig. 4b shows the absolute value of the upper-left portion of unfiltered matrix Ξ, which is representative of the correlation between the ith temporal mode of the probes and the jth temporal mode of the flow field, with i and j being respectively the row and column numbers in Ξ. The matrix Ξ shows a clear diagonal dominance for at least the first 100 modes, which indicates a strong direct correspondence between probe and field modes. As the mode number is increased, this dominance disappears and each probe mode tends to correspond to a larger number of field modes.

The performances of EPOD are reported in Fig. 5 for a single snapshot of the testing dataset, both in terms of 2-component flow field

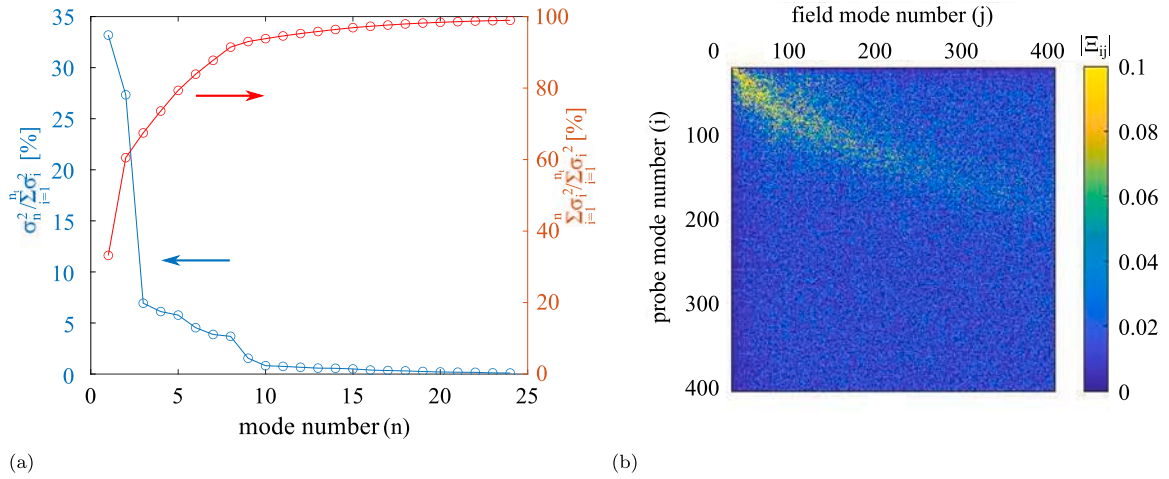

Fig. 4. (**a**) Energy distribution (blue, arrow toward left) and cumulative energy (red, arrow toward right) in the first 24 POD modes of the flow field; (**b**) absolute value of Ξ for the fluidic pinball test case (first 400 × 400 entries).

and pressure. The DNS data are presented for comparison (Fig. 5a–c), while the velocity field and pressure estimation, without filter (Fig. 5d–f), with Ξ-filter (Fig. 5g–i) and with ψ-filter (Fig. 5j–l) are also reported in this figure. The estimation error of the velocity and pressure fields of Fig. 5 with respect to the DNS data is reported in Fig. 6 for the unfiltered EPOD (Fig. 6a–c), the Ξ-filtered EPOD (Fig. 6d–f) and the ψ-filtered EPOD (Fig. 6g–i). The EPOD reconstructs the velocity field and estimates the pressure field with relatively-high fidelity. The error mainly affects the streamwise velocity component in the wake region (from $x = 2D$ to $x = 4D$), producing an error pattern which suggests the misplacement of flow structures in the y-direction. The crosswise velocity component shows lower levels of error, still localized in the same region. The localization of the reconstruction error might be an effect of the presence of intense flow features, strongly subjected to stretching and deformation, and for which Taylor's hypothesis is not accurate, thus affecting the performances of the virtual-probe approach. Additionally, this region stands farther from the probes. These two aspects contribute in the reduced capability of the probes to sense accurately the fluctuations in this region. Nonetheless, the pressure reconstruction has acceptable levels of estimation error, suggesting that the integration is smoothing down the error in the spatial derivatives. The unfiltered and ψ-filtered EPOD both show low levels of error, while the Ξ-filtered EPOD introduces slightly larger error, since some information is filtered out by the Ξ-filter.

A further quantitative assessment of the estimation error has been carried out over a testing dataset of 1500 snapshots by computing the Root Mean Square (RMS) error with respect to the original DNS fields. The assessment includes also the estimation through the TH, which is, to date, the most common option to estimate time-derivatives from planar snapshot PIV [8]. This method enables the estimation of the time derivative of velocity, and thus of the pressure, for a measured snapshot. This approach will be referred to as *in-sample TH* in the remainder of this paper. A Gaussian spatial filter with standard deviation equal to 7 vectors on a kernel of 29 × 29 vectors has been applied to the local velocity inside the measured snapshot to provide the convection velocity $\mathbf{u}_c$. Additionally, the TH can be used to propagate the measured frame in time, obtaining an estimated time-resolved sequence of velocity fields. The simplest way to fulfill it is by means of a unidirectional Euler propagation, which is

$$\begin{aligned}\mathbf{u}(t_0 + dt) &= \mathbf{u}(t_0) + \left.\frac{\partial u}{\partial t}\right|_{t_0} dt \\ &= \mathbf{u}(t_0) - (\mathbf{u}_c \cdot \nabla)\mathbf{u}'(t_0)dt\end{aligned} \tag{11}$$

in the present case, where the convective velocity $\mathbf{u}_c$ is the spatially-filtered velocity inside the snapshot, and the time-resolved sequence has been estimated with TH using a 4th order Runge–Kutta method with unidirectional propagation. This approach will be referred to as *out-of-sample TH* in the remainder of this paper. It should be noted that the error comes from both the absence of inlet information and its accumulation in the propagation process.

Fig. 7 shows the RMS estimation error for the unfiltered EPOD estimation (Fig. 7a–c), the Ξ-filtered EPOD estimation (Fig. 7d–f), the ψ-filtered EPOD (Fig. 7g–i) and the estimation using the TH. The error on the streamwise component of velocity is reported in the left column (Fig. 7a,d,g), the error on the time-derivative on the streamwise component of velocity in the central column (Fig. 7b,e,h,j) and the error on pressure in the right column (Fig. 7c,f,i,k). For the TH, the estimation has been carried out in the least error conditions, i.e. assuming that the exact velocity field was available at the selected snapshot, thus using the in-sample TH to estimate only the time derivative. Despite the velocity estimation from the unfiltered EPOD (Fig. 7a) has reasonable levels of error, the pressure estimation (Fig. 7c) is affected by large errors. This is mainly produced by the time derivative of the velocity (Fig. 7b), which significantly amplifies the spurious fluctuations in the POD temporal modes. Similar levels of error are present in the pressure estimation from the TH (Fig. 7k), also in this case produced by large errors in the time derivative (Fig. 7j). The Ξ-filtered EPOD, instead, produces slightly worse results in terms of estimated velocity fields (Fig. 7d), but shows much lower errors on the time derivative (Fig. 7e) and, thus, on the pressure estimation (Fig. 7f). The results of the ψ-filtered EPOD shows the lowest levels of error both in term of velocity-field estimation (Fig. 7g) and of its time derivative (Fig. 7h), which lead to relatively low errors in the pressure estimation (Fig. 7i). It should be mentioned that time filtering may smear out high-frequency fluctuations. Nonetheless, such scales have smaller turnover times, and so are less likely to exhibit correlation with the probe data, thus the estimation process is already partially filtering their intensity. In any case, the Butterworth filter should be carefully tuned not to alter the largest scale motions, which contain most of the energy and are well retained by the most energetic POD modes and by the estimation process.

It is worthwhile remarking that the EPOD estimation, differently from the TH, provides by default a set of time-resolved velocity fields, thus it can be employed to estimate full time-series of velocity and pressure fluctuations. Taylor's hypothesis, by contrast, is generally employed to estimate the time-derivative in a measured flow-field snapshot (in-sample TH); when used to propagate the velocity fields over time (out-of-sample TH), the estimation error increases rapidly. To clarify it, the RMS error of the estimated pressure in the whole domain is plotted in Fig. 8a over 0.32 non-dimensional through-time

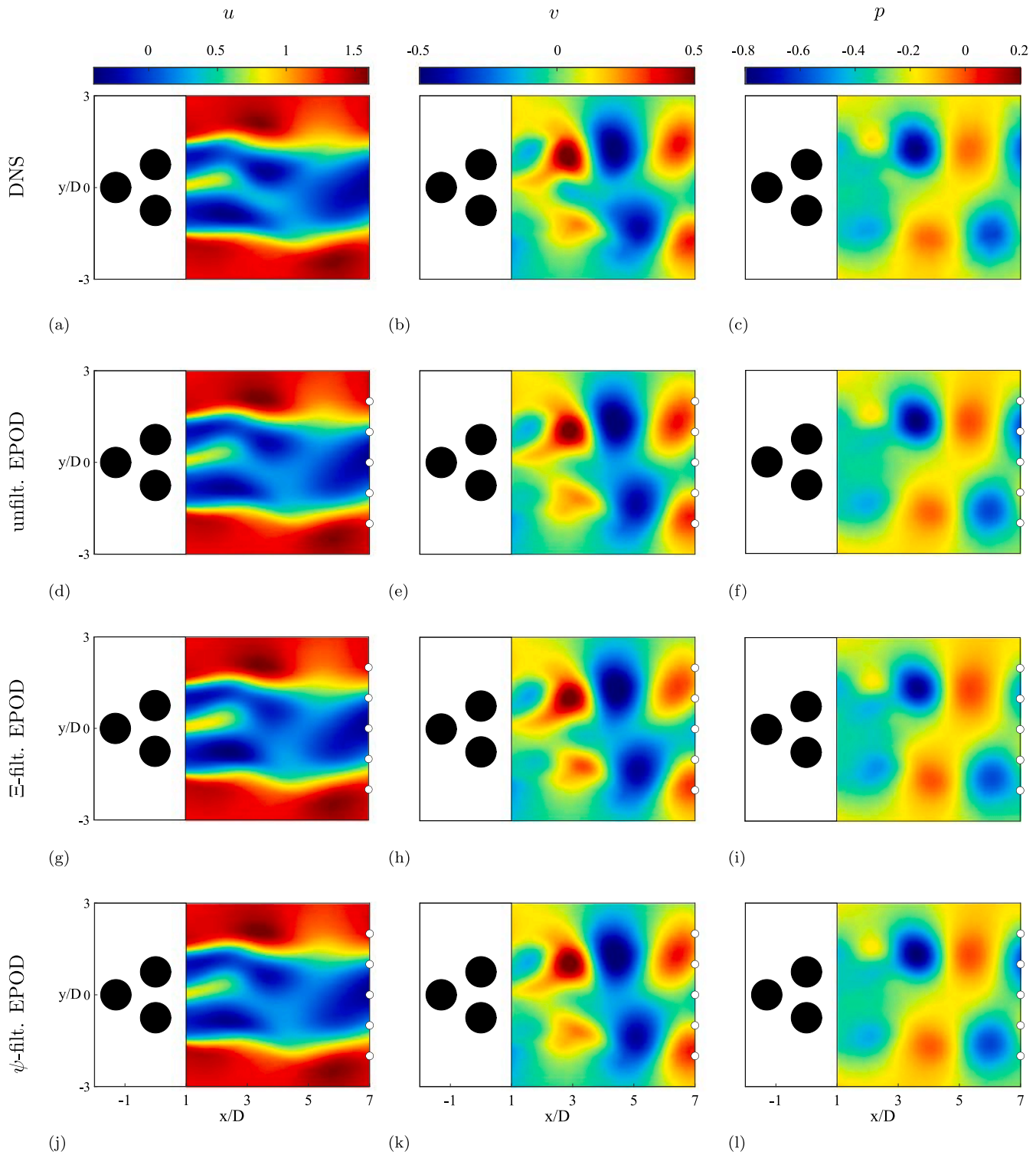

Fig. 5. Exact and estimated velocity and pressure fields for a single snapshot: (**a**) streamwise velocity from DNS; (**b**) crosswise velocity from DNS; (**c**) pressure from DNS; (**d**) streamwise velocity from non-filtered EPOD; (**e**) crosswise velocity from non-filtered EPOD; (**f**) pressure from non-filtered EPOD; (**g**) streamwise velocity from Ξ-filtered EPOD; (**h**) crosswise velocity from Ξ-filtered EPOD; (**i**) pressure from Ξ-filtered EPOD; (**j**) streamwise velocity from ψ-filtered EPOD; (**k**) crosswise velocity from ψ-filtered EPOD; (**l**) pressure from ψ-filtered EPOD.

(20 frames) from the beginning of the propagation. In this paper, one unitary non-dimensional through-time t^* is defined as L/U_∞, where L is the domain length, and U_∞ is the freestream velocity. The results are compared to the in-sample TH-based pressure estimation. The ψ-filtered EPOD estimation is the most accurate method to reconstruct time-resolved flow and pressure field series among the tested set of techniques. The error of in-sample TH is larger than EPOD, but remains stable around a fixed value through time. The error of out-of-sample TH is similar to in-sample TH for $\Delta t^* < 0.1$ and starts to grow quickly after that point.

In order to assess the robustness of the estimation in presence of noise, the RMS error of the estimated pressure in the whole domain

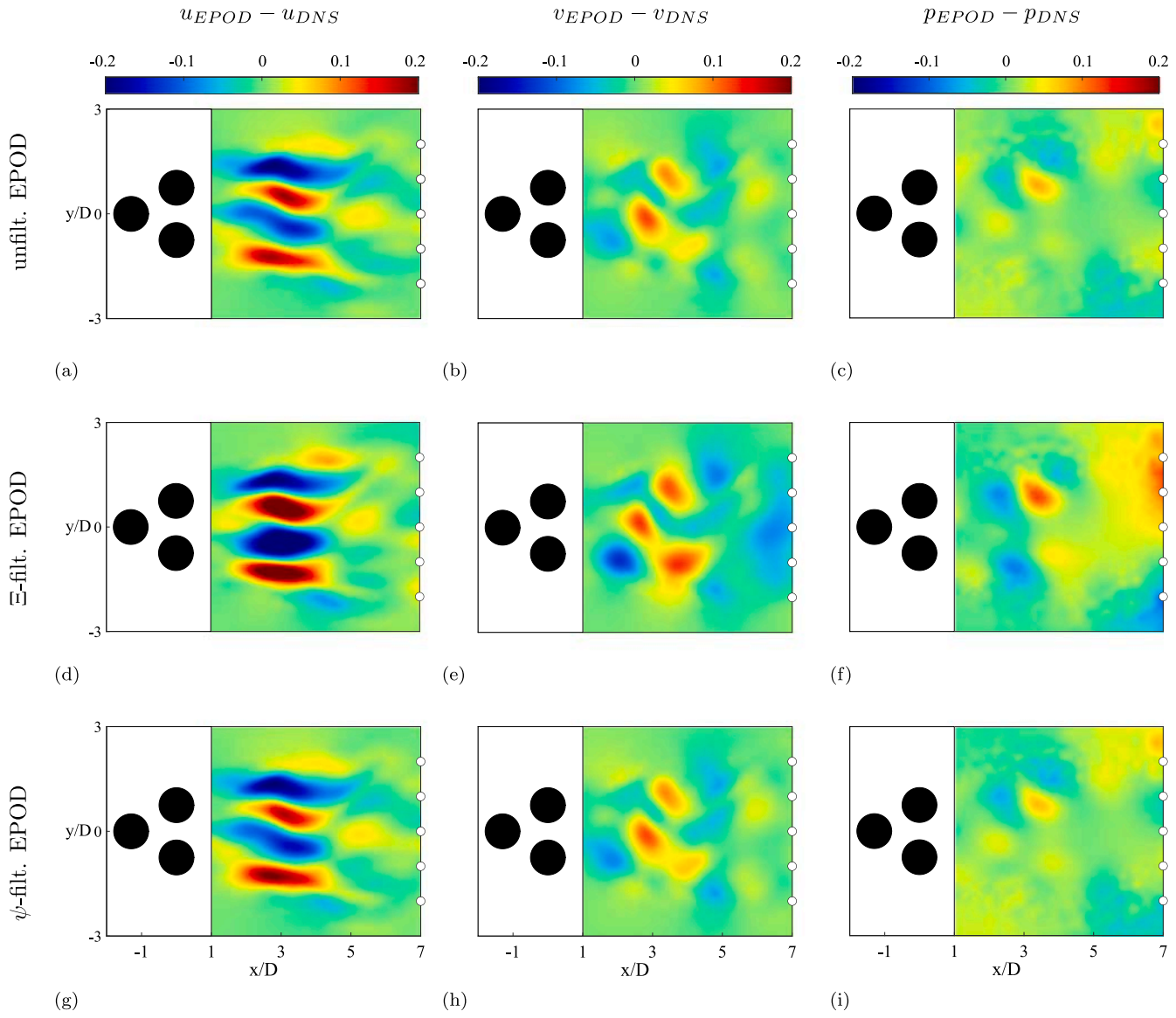

Fig. 6. Error of estimated velocity and pressure fields for a single snapshot: (**a**) streamwise velocity from non-filtered EPOD; (**b**) crosswise velocity from non-filtered EPOD; (**c**) pressure from non-filtered EPOD; (**d**) streamwise velocity from Ξ-filtered EPOD; (**e**) crosswise velocity from Ξ-filtered EPOD; (**f**) pressure from Ξ-filtered EPOD; (**g**) streamwise velocity from ψ-filtered EPOD; (**h**) crosswise velocity from ψ-filtered EPOD; (**i**) pressure from ψ-filtered EPOD.

within $0 < \Delta t^* < 1/6$ is reported in Fig. 8b for different levels of noise in the training data and in the probe data used for testing, applying the same methods as in Fig. 8a. Gaussian noise with zero mean value and standard deviation up to 4% of the freestream velocity is superposed to both velocity components. The ψ-filtered EPOD estimation has significant less error in the pressure estimation than TH (whether is in-sample or not) for all the tested noise levels. By contrast, the propagated TH error diverges very quickly as soon as the noise level is higher than 0.5% of the freestream velocity.

4.2. Channel flow

The proposed method is validated using a second synthetic dataset extracted from the DNS of a channel flow contained in the Johns Hopkins Turbulence Databases [26,40]. Owing to the higher spectral richness of the flow, this test case is expected to be more challenging for the EPOD estimation than the shedding-dominated wake flow of the pinball test case. The DNS is solved in a domain of size $8\pi h \times 2h \times 3\pi h$ (with $h = 1$ being the half-channel height), using 2048 x 512 x 1536 nodes, at friction-velocity-based Reynolds number $Re_\tau \approx 1000$, and the time interval for storage is 0.0065. The EPOD estimation is evaluated in a training dataset composed by sub-domains in streamwise/wall-normal (indicated respectively as x/y) planes of size $h \times h$, the grid spacing is set to be $0.0114h$ thus every sub-domain includes 88×88 2-component velocity vectors. The sub-domains are extracted from different positions in the spanwise and streamwise directions of the channel exploiting statistical homogeneity to collect enough independent snapshots, similarly as to what reported in [16]. The data for training are sampled with a time interval of 2/3 convection throughtime thus being non-time-resolved, i.e. fluid parcels moving at bulk velocity displace $2/3h$ in x direction in the time between 2 snapshots. For simplicity we will consider that the streamwise coordinate x spans between 0 and h, although we are actually considering domains at different streamwise locations, and y direction to be between 0 and h where 0 is the wall position. Additionally, the dataset includes 10 probes measuring the 2 in-plane components of velocity placed along the downstream edge of the sub-domain spaced of $0.1h$ in the wall-normal direction y and recording 152 samples for each snapshot with a time-spacing of 0.0065, thus covering one subdomain convection throughtime.

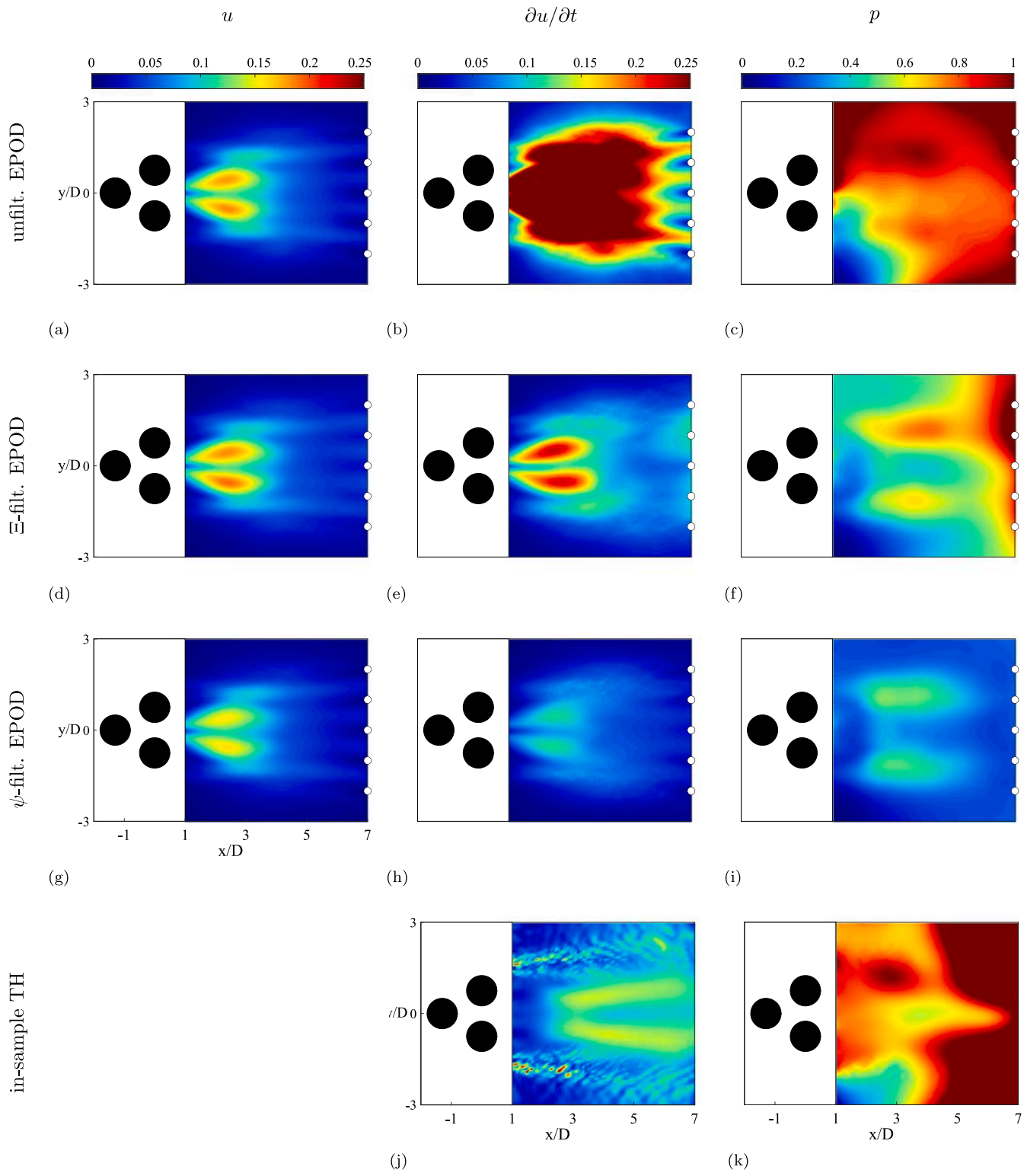

Fig. 7. RMS error map of velocity and pressure fields estimation using the EPOD without filter, the Ξ-filtered EPOD, the Ψ-filtered EPOD and the Taylor's hypothesis. The first column shows error on the streamwise velocity, the second column shows the one on the time derivative of streamwise velocity, and the last column shows the error on pressure.

The RMS error map of the pressure using the ψ-filtered EPOD estimation and the Taylor's hypothesis (both in-sample and out-of-sample) are shown in Fig. 9. The EPOD for this case is trained on 6400 snapshots. The testing dataset, instead, is composed by 240 time-resolved frames, statistically uncorrelated to the training dataset. In fact, the training dataset is built using data only from one half channel, while the testing dataset is extracted from the other half. Unlike the fluidic pinball case, Taylor's hypothesis (Fig. 9b) performs better than the EPOD estimation (Fig. 9a), especially in the near wall region ($0 < y < 0.3h$) and in the upstream boundary of the domain ($0 < x < 0.1h$). The higher error of the EPOD might be explained by several reasons. Firstly, the channel flow reported here is characterized by a moderate Reynolds

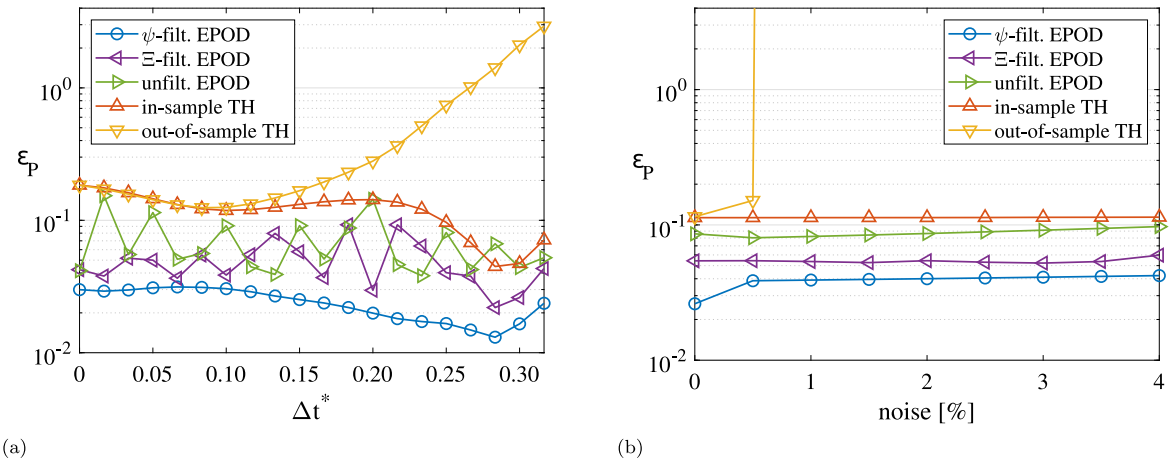

Fig. 8. (**a**) RMS error of estimated pressure over the whole domain as propagates in time after the measured frame, where $\Delta t^* = 0$ is the position of in-sample snapshot for out-of-sample TH. (**b**) RMS error of estimated pressure over the whole domain for different levels of noise in training data, the out-of-sample TH is the average in $\Delta t^* < 1/6$. legends: ψ-filtered EPOD (blue circles), Ξ-filtered EPOD (purple leftward triangles), un-filtered EPOD (green rightward triangles), in-sample TH (red upward triangles) and out-of-sample TH (yellow downward triangles).

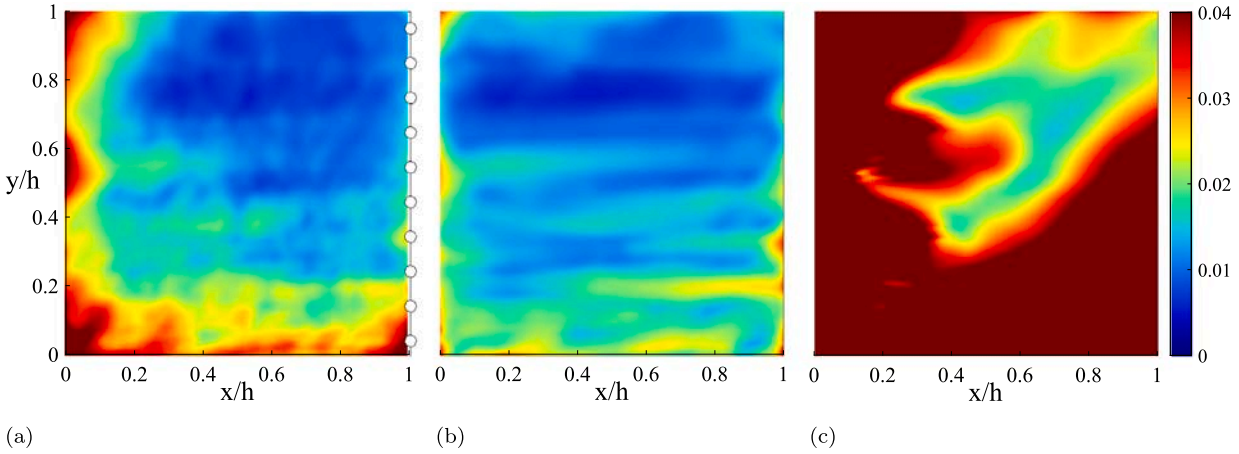

Fig. 9. RMS error map of velocity and pressure fields estimation using (**a**) ψ-filtered EPOD estimation, (**b**) in-sample Taylor's hypothesis, (**c**) out-of-sample Taylor's hypothesis, averaging for $0 < \Delta t^* < 0.52$.

number, thus being completely turbulent and having a much larger wealth of turbulent scales (generally recovered by a larger number of POD modes), lowering the correlation between field and probe modes. Secondly, larger turbulence introduces stronger three-dimensionality in the flow, thus further reducing the correlation level. Thirdly, the channel is characterized by much lower convection velocity in the near-wall region. This means that in the temporal span recorded by the fast probes (roughly one convection throughtime, i.e. the time required by a fluid particle to span the entire sub-domain when convected at the bulk velocity) is not long enough to sense all the fluid structures passing. Finally, the near-wall region is characterized by a stronger deformation of the small-scale fluid structures as well as by their interaction with larger structures, meaning that the correlation between the field modes and probe modes is lower. Despite this, the EPOD estimation offers reasonably good results in terms of pressure (Fig. 9a). Additionally, as discussed in the previous section, EPOD estimation offers an inherent advantage with respect to the TH in that it provides time-series for tracking the fluctuations of pressure and velocity in time. While this can be achieved also by the out-of-sample TH, the RMS error of such estimation from a measured in-sample snapshot at $\Delta t^* = 0$ to half convection throughtime (Fig. 9c) contains high error levels, which further increase for increasing time separation.

Fig. 10a compares the EPOD estimation and the Taylor's hypothesis in recovering time-series out of an initial snapshot in terms of RMS pressure estimation error over the sub-domain. As already commented, in the channel flow, the estimation of in-sample TH is superior to the EPOD approach. However, the error of out-of-sample TH increases quickly with time. On the other hand, the EPOD approach maintains stable levels of error throughout all the time sequence, producing better results than the out-of-sample TH after 20 steps, which corresponds to $\Delta t^* = 0.13$. Fig. 10b reports the RMS error of the pressure in the whole sub-domain and over the first 10 snapshot of propagation with different levels of noise on the velocity field data. The in-sample TH proves to be the most robust one to noise. EPOD, regardless of the filtering method used, has a rather constant error independently of the noise level within the tested range (the unfiltered EPOD has only slightly increasing error with noise level). The out-of-sample TH, instead, has an error which increases with the noise, proving to provide the least robust pressure time-series estimation.

5. Experimental test on the wake of a wing

The proposed method is tested on an experimental dataset of a PIV measurement in the wake of a 2D wing with a NACA 0018 airfoil. The experiment is carried out in the water tunnel of the Universidad Carlos III de Madrid, which has a $2.5 \times 0.5 \times 0.55$ m^3 test section. The wing has 80 mm chord length, and the freestream velocity is tuned to $U_\infty = 0.06$ m/s, thus resulting in a Reynolds number of approximately

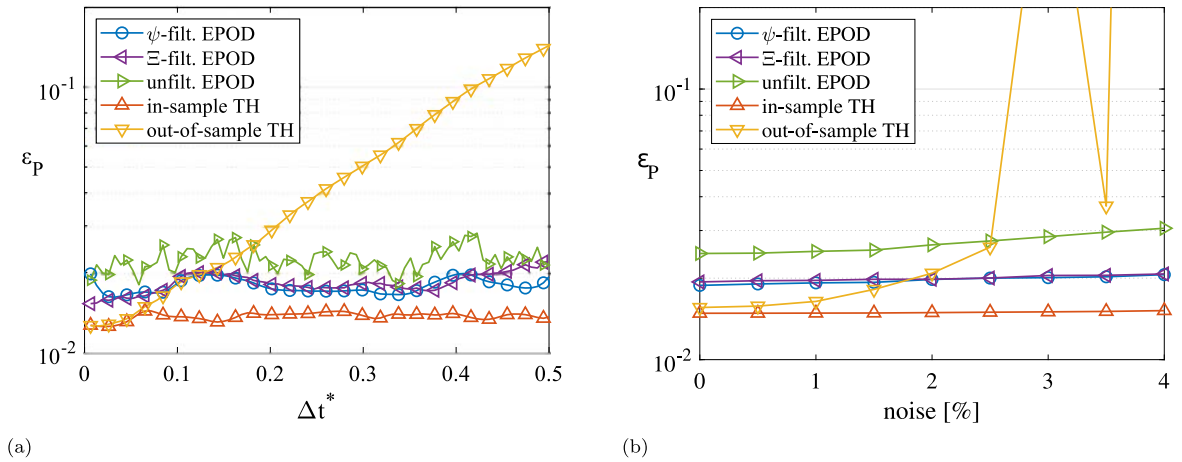

Fig. 10. (**a**) RMS error of estimated pressure over the whole domain as propagates in time after the measured frame. (**b**) RMS error of estimated pressure over the whole domain under different levels of noise in training data and probes input. The out-of-sample TH is calculated in $\Delta t^* < 0.065$. ψ-filtered EPOD (blue circles), Ξ-filtered EPOD (purple leftward triangles), un-filtered EPOD (green rightward triangles), in-sample TH (red upward triangles) and out-of-sample TH (yellow downward triangles).

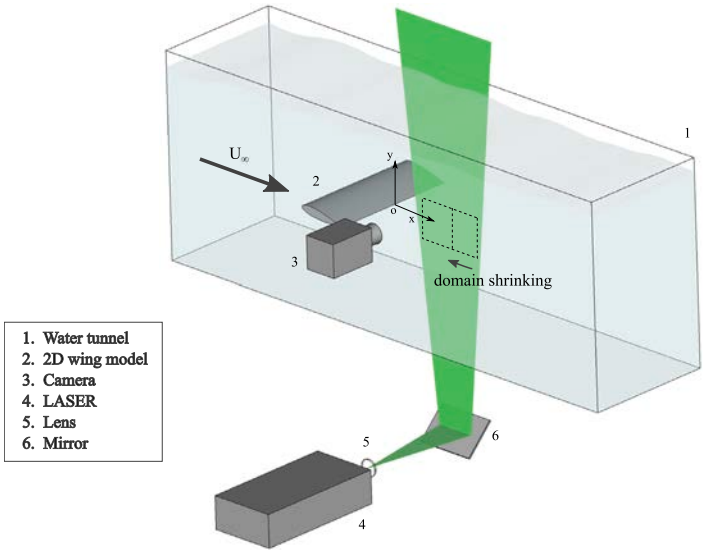

Fig. 11. Sketch of experimental setting.

4800. The wing is mounted with an angle of attack of 10° to generate a moderate-intensity shedding wake.

As shown in Fig. 11, a dual cavity pulsed Nd:YAG Quantel Evergreen laser lights an approximately 1mm-thick sheet after reshaping the laser beam via a spherical and a cylindrical lens. An Andor sCMOS camera with 2560×2160 px^2 sensor (with pixel pitch of 6.5 μm) is used as recording device. The camera is equipped with a 50 mm focal length objective, and set to a resolution of 8.3 px/mm. The flow is seeded with neutrally-bouyant polymide particles with 56 μm diameter. Particle images are sampled at 30 Hz, which is sufficient to obtain time-resolved measurements, being the particle displacement in the freestream within frames equal to approximately 16 pixels. A sliding correlation [41] with 3-frame kernel is applied and the final interrogation window size is 40 px with 75% overlap, resulting in a vector spacing of 1.20 mm.

The training dataset for EPOD is composed of 334 velocity fields captured at 1 Hz, i.e. downsampling by a factor of 30 the original sequence. Artificial probes with higher temporal resolution are built by using the original sequence with sampling frequency at 30 Hz. This approach for testing is similar to the one proposed by Tu et al. [15]. The complete PIV domain spans $1.6c$ in the streamwise direction, starting at approximately $0.75c$ from the trailing edge. Eleven probes are set on the downstream edge of the domain, and the velocity reconstruction is performed with the ψ-filtering method, which has shown in the synthetic test cases to provide the best results. The selected timespan associated to each physical probe is set equal to one convective throughtime within the domain, so it is adjusted accordingly for different domain width.

The pressure from the original time-resolved sequence, EPOD-estimated fields with ψ-filtering, in-sample Taylor's hypothesis and out-of-sample propagation from the previous snapshot in training set are compared in Fig. 12. The results from velocity fields estimated with EPOD show a good trend of high and low-pressure area, and the result is qualitatively good in the near wake region, while larger errors are observed at the boundaries of the domain. In-sample Taylor's hypothesis shows large errors and a significant smoothing of the pressure fluctuations.

Since it is expected that errors in velocity estimation become larger for points far from the probes, we tested the effect of the domain length on the accuracy of the estimated pressure using EPOD. The domain is cropped to different sizes in the streamwise direction (from $0.8c$ to $1.6c$) to test the effect of the distance of the probes from the region to estimate. As sketched in Fig. 11, the upstream, bottom and top edges are kept fixed, while the downstream edge is moved to span

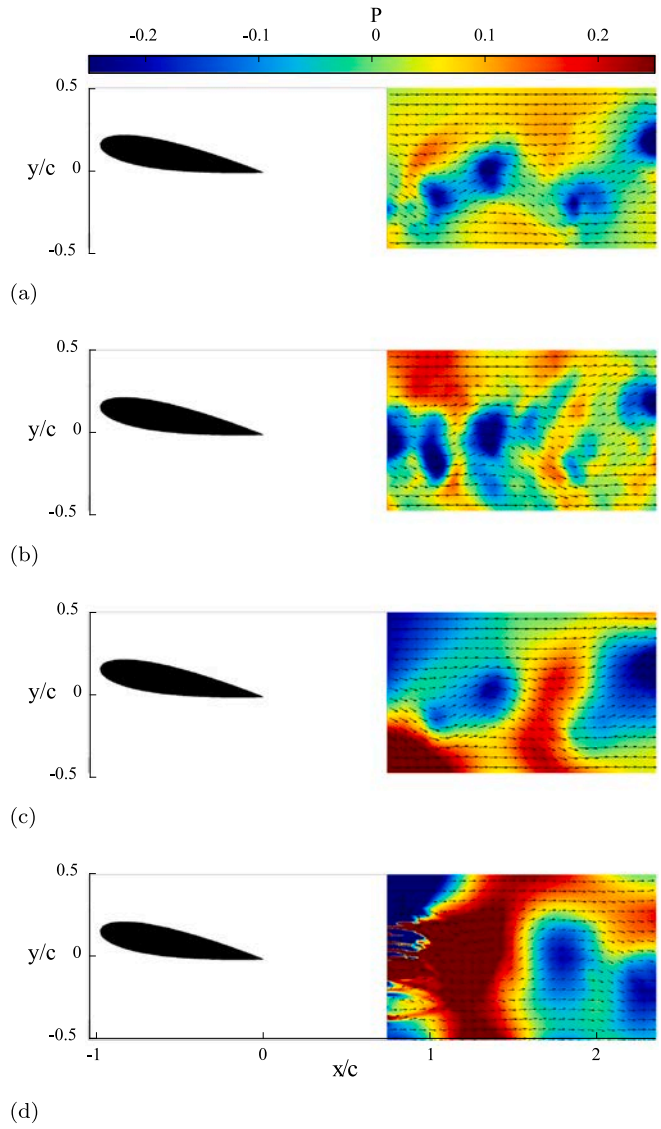

Fig. 12. Non-dimensional instantaneous pressure field from: (**a**) time-resolved PIV; (**b**) EPOD reconstruction with ψ-filtering; (**c**) in-sample Taylor's hypothesis: (**d**) out-of-sample Taylor's hypothesis, after the propagation of $\Delta t^* = 0.48$ from sample snapshot.

different domain lengths. In all cases the probes are located at the downstream end of the domain, which is a natural choice to minimize intrusiveness. The RMS error in estimating velocity fields is shown for different domain lengths L, expressed in non-dimensional form. Fig. 13 compares the RMS error of velocity (Fig. 13a) and pressure (Fig. 13b) from EPOD, in-sample and out-of-sample Taylor's hypothesis. EPOD improves slightly with the domain shrinking, while the Taylor's hypothesis does not benefit from it in pressure estimation accuracy. The reason behind the increase of the error with domain shrinking is that in the upstream portion of the domain the shear intensity is higher, thus Taylor's hypothesis holds poorly. As a result, EPOD surpass Taylor's hypothesis when the domain length is under $1.3c$. It can be seen that the wake flow near the wing has more small-scale motion and turbulence production, thus Taylor's hypothesis sometimes fails to predict time-derivative of velocity from single snapshot. For the EPOD, the problem is that the fluid structures undergo a significant evolution before reaching the probes, but this issue is reduced by shrinking the domain. For the case of out-of-sample Taylor-hypothesis propagation, the error increases rapidly with the time separation, being EPOD superior to it for non-dimensional throughtime separation larger than 0.3 for all selected domain lengths.

6. Summary and conclusions

A novel approach to estimate instantaneous pressure fields using snapshot PIV (i.e. without time resolution) has been presented. The method is based on synchronized field measurements from PIV and point measurements using high-repetition rate probes (such as hot-wires or pressure transducers, among others). The fields are then estimated at the same time resolution of the probes using extended POD, and the pressure gradient is extracted from the Navier–Stokes equations and integrated in space. The method has demonstrated to be sufficiently accurate to perform this task. The results show that EPOD is superior to Taylor's hypothesis if the POD reconstruction is sufficiently compact, and provided that temporal filtering is applied to reduce noise. While the method seems to be less accurate than enforcement of the Taylor's hypothesis in flows where this approximation works well, it has shown to have several appealing features:

- It is a model-free method, thus it does not require to impose convection velocity or any model-based constraint. This renders the proposed approach particularly suitable in flows with compact POD spectrum, and has better pressure prediction than a model-based method such as Taylor's hypothesis. Besides, this data-driven method may still work when sufficiently accurate models are difficult to infer a priori.
- Once performed the training, only probe data are needed to estimate the fields, thus allowing to encode large sequences of velocity and pressure fields with minimal data rate burden.
- The error of the method is independent on whether the estimation is done in-sample or out-of-sample (provided that the in-sample estimation is carried out over the testing dataset). This ensures a relatively uniform level of error, while model-based methods are characterized by increasing error with time separation from the starting sample of the sequence.

It is worth highlighting that, in this proof-of-concept study, the estimation method is rather simple. More sophisticated architectures have already shown to outperform EPOD. It is to be expected that future advances in machine learning will foster accurate and reliable estimation methods which can be the substrate for pushing the capabilities of the method proposed here for pressure field estimation.

CRediT authorship contribution statement

Junwei Chen: Methodology, Software, Validation, Investigation, Data Curation, Writing – original draft, Writing – review & editing, Visualization. **Marco Raiola:** Methodology, Software, Investigation, Writing – original draft, Writing – review & editing, Visualization, Supervision. **Stefano Discetti:** Conceptualization, Methodology, Investigation, Writing – original draft, Writing – review & editing, Supervision, Funding acquisition.

Declaration of competing interest

The authors declare that they have no known competing financial interests or personal relationships that could have appeared to influence the work reported in this paper.

Data and code availability statement

All dataset used in this work are openly available in Zenodo, accessible at https://doi.org/10.5281/zenodo.6473075. All codes developed in this work are openly available in GitHub, accessible through the link: https://github.com/erc-nextflow/Data-driven-pressure-estimation-with-EPOD.

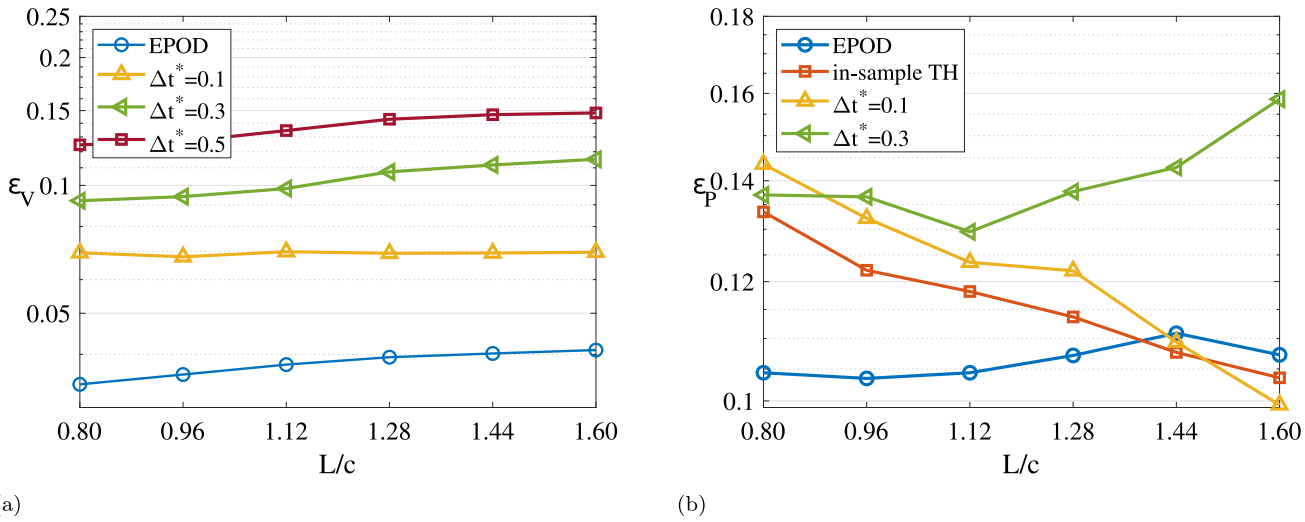

Fig. 13. RMS error of velocity and pressure estimation at the domain length from $0.8c$ to $1.6c$. (**a**) RMS error of non-dimensional velocity achieved from ψ-filtered EPOD, and out-of-sample TH in three different propagation time, (**b**) RMS error of non-dimensional pressure using EPOD, in-sample TH, out-of-sample TH propagated during $\Delta t^* = 0.1$ and 0.3.

Acknowledgments

This project has received funding from the European Research Council (ERC) under the European Union's Horizon 2020 research and innovation program (grant agreement No 949085). Funding for APC: Universidad Carlos III de Madrid (Read & Publish Agreement CRUE-CSIC 2022). The authors warmly acknowledge M. Morzynski and B. Noack for providing access to the fluidic pinball DNS code.

References

[1] C. Tropea, A.L. Yarin, J.F. Foss, et al., Springer Handbook of Experimental Fluid Mechanics, Vol. 1, Springer, 2007.
[2] B. Van Oudheusden, PIV-based pressure measurement, Meas. Sci. Technol. 24 (3) (2013) 032001.
[3] P. Van Gent, D. Michaelis, B. Van Oudheusden, P.-E. Weiss, R. de Kat, A. Laskari, Y.J. Jeon, L. David, D. Schanz, F. Huhn, et al., Comparative assessment of pressure field reconstructions from particle image velocimetry measurements and Lagrangian particle tracking, Exp. Fluids 58 (4) (2017) 33.
[4] R. Gurka, A. Liberzon, D. Hefetz, D. Rubinstein, U. Shavit, Computation of pressure distribution using PIV velocity data, in: Workshop on Particle Image Velocimetry, Vol. 2, 1999, pp. 1–6.
[5] S. Hosokawa, S. Moriyama, A. Tomiyama, N. Takada, PIV measurement of pressure distributions about single bubbles, J. Nucl. Sci. Technol. 40 (10) (2003) 754–762.
[6] R. de Kat, B. Ganapathisubramani, Pressure from particle image velocimetry for convective flows: a Taylor's hypothesis approach, Meas. Sci. Technol. 24 (2) (2012) 024002.
[7] A. Laskari, R. de Kat, B. Ganapathisubramani, Full-field pressure from snapshot and time-resolved volumetric PIV, Exp. Fluids 57 (3) (2016) 44.
[8] J. Van der Kindere, A. Laskari, B. Ganapathisubramani, R. De Kat, Pressure from 2D snapshot PIV, Exp. Fluids 60 (2) (2019) 32.
[9] J.F. Schneiders, S. Pröbsting, R.P. Dwight, B.W. van Oudheusden, F. Scarano, Pressure estimation from single-snapshot tomographic PIV in a turbulent boundary layer, Exp. Fluids 57 (4) (2016) 53.
[10] J. Borée, Extended proper orthogonal decomposition: a tool to analyse correlated events in turbulent flows, Exp. Fluids 35 (2) (2003) 188–192.
[11] R.J. Adrian, Stochastic estimation of conditional structure: a review, Appl. Sci. Res. 53 (3) (1994) 291–303.
[12] C. Tinney, L. Ukeiley, M.N. Glauser, Low-dimensional characteristics of a transonic jet. Part 2. Estimate and far-field prediction, J. Fluid Mech. 615 (2008) 53–92.
[13] Z. Hosseini, R.J. Martinuzzi, B.R. Noack, Sensor-based estimation of the velocity in the wake of a low-aspect-ratio pyramid, Exp. Fluids 56 (1) (2015) 13.
[14] J. Bourgeois, B. Noack, R. Martinuzzi, Generalized phase average with applications to sensor-based flow estimation of the wall-mounted square cylinder wake, J. Fluid Mech. 736 (2013) 316–350.
[15] J.H. Tu, J. Griffin, A. Hart, C.W. Rowley, L.N. Cattafesta, L.S. Ukeiley, Integration of non-time-resolved PIV and time-resolved velocity point sensors for dynamic estimation of velocity fields, Exp. Fluids 54 (2) (2013) 1–20.
[16] S. Discetti, M. Raiola, A. Ianiro, Estimation of time-resolved turbulent fields through correlation of non-time-resolved field measurements and time-resolved point measurements, Exp. Therm Fluid Sci. 93 (2018) 119–130.
[17] S. Discetti, G. Bellani, R. Örlü, J. Serpieri, C.S. Vila, M. Raiola, X. Zheng, L. Mascotelli, A. Talamelli, A. Ianiro, Characterization of very-large-scale motions in high-Re pipe flows, Exp. Therm Fluid Sci. 104 (2019) 1–8.
[18] N.B. Erichson, L. Mathelin, Z. Yao, S.L. Brunton, M.W. Mahoney, J.N. Kutz, Shallow neural networks for fluid flow reconstruction with limited sensors, Proc. R. Soc. Lond. Ser. A Math. Phys. Eng. Sci. 476 (2238) (2020) 20200097.
[19] A. Güemes, S. Discetti, A. Ianiro, Sensing the turbulent large-scale motions with their wall signature, Phys. Fluids 31 (12) (2019) 125112.
[20] L. Guastoni, A. Güemes, A. Ianiro, S. Discetti, P. Schlatter, H. Azizpour, R. Vinuesa, Convolutional-network models to predict wall-bounded turbulence from wall quantities, J. Fluid Mech. 928 (2021).
[21] A. Guemes, S. Discetti, A. Ianiro, B. Sirmacek, H. Azizpour, R. Vinuesa, From coarse wall measurements to turbulent velocity fields through deep learning, Phys. Fluids 33 (7) (2021).
[22] Z. Deng, Y. Chen, Y. Liu, K.C. Kim, Time-resolved turbulent velocity field reconstruction using a long short-term memory (LSTM)-based artificial intelligence framework, Phys. Fluids 31 (7) (2019) 075108.
[23] A. Giannopoulos, J.-L. Aider, Data-driven order reduction and velocity field reconstruction using neural networks: The case of a turbulent boundary layer, Phys. Fluids 32 (9) (2020) 095117.
[24] X. Jin, S. Laima, W.-L. Chen, H. Li, Time-resolved reconstruction of flow field around a circular cylinder by recurrent neural networks based on non-time-resolved particle image velocimetry measurements, Exp. Fluids 61 (4) (2020) 1–23.
[25] N. Deng, B.R. Noack, M. Morzyński, L.R. Pastur, Low-order model for successive bifurcations of the fluidic pinball, J. Fluid Mech. 884 (2020).
[26] Y. Li, E. Perlman, M. Wan, Y. Yang, C. Meneveau, R. Burns, S. Chen, A. Szalay, G. Eyink, A public turbulence database cluster and applications to study Lagrangian evolution of velocity increments in turbulence, J. Turbul. 9 (2008) N31.
[27] D. Ewing, J.H. Citriniti, Examination of a LSE/POD complementary technique using single and multi-time information in the axisymmetric shear layer, in: IUTAM Symposium on Simulation and Identification of Organized Structures in Flows, Springer, 1999, pp. 375–384.
[28] C. Tinney, F. Coiffet, J. Delville, A. Hall, P. Jordan, M. Glauser, On spectral linear stochastic estimation, Exp. Fluids 41 (5) (2006) 763–775.
[29] C. Sicot, R. Perrin, T. Tran, J. Borée, Wall pressure and conditional flow structures downstream of a reattaching flow region, Int. J. Heat Fluid Flow 35 (2012) 119–129.
[30] M. Ghil, M. Allen, M. Dettinger, K. Ide, D. Kondrashov, M. Mann, A.W. Robertson, A. Saunders, Y. Tian, F. Varadi, et al., Advanced spectral methods for climatic time series, Rev. Geophys. 40 (1) (2002) 3–1.
[31] V. Durgesh, J. Naughton, Multi-time-delay LSE-POD complementary approach applied to unsteady high-Reynolds-number near wake flow, Exp. Fluids 49 (3) (2010) 571–583.
[32] Y. Murai, T. Nakada, T. Suzuki, F. Yamamoto, Particle tracking velocimetry applied to estimate the pressure field around a savonius turbine, Meas. Sci. Technol. 18 (8) (2007) 2491.
[33] Y.J. Jeon, G. Gomit, T. Earl, L. Chatellier, L. David, Sequential least-square reconstruction of instantaneous pressure field around a body from TR-PIV, Exp. Fluids 59 (2) (2018) 1–15.

[34] T. Baur, J. Köngeter, PIV with high temporal resolution for the determination of local pressure reductions from coherent turbulent phenomena, in: 3rd Int. Workshop on Particle Image Velocimetry, 1999, pp. 101–106.
[35] X. Liu, J. Katz, Instantaneous pressure and material acceleration measurements using a four-exposure PIV system, Exp. Fluids 41 (2) (2006) 227–240.
[36] X. Liu, J.R. Moreto, S. Siddle-Mitchell, Instantaneous pressure reconstruction from measured pressure gradient using rotating parallel ray method, in: 54th AIAA Aerospace Sciences Meeting, 2016, p. 1049.
[37] X. Liu, J.R. Moreto, Error propagation from the PIV-based pressure gradient to the integrated pressure by the omnidirectional integration method, Meas. Sci. Technol. 31 (5) (2020) 055301.
[38] T. Tronchin, L. David, A. Farcy, Loads and pressure evaluation of the flow around a flapping wing from instantaneous 3D velocity measurements, Exp. Fluids 56 (7) (2015).
[39] L.F. Richardson, The approximate arithmetical solution by finite differences of physical problems involving differential equations, with an application to the stresses in a masonry dam, Phil. Trans. R. Soc. A 210 (1910) 307.
[40] H. Yu, K. Kanov, E. Perlman, J. Graham, E. Frederix, R. Burns, A. Szalay, G. Eyink, C. Meneveau, Studying Lagrangian dynamics of turbulence using on-demand fluid particle tracking in a public turbulence database, J. Turbul. 13 (2012) N12.
[41] F. Scarano, P. Moore, An advection-based model to increase the temporal resolution of PIV time series, Exp. Fluids 52 (4) (2012) 919–933.